International Journal of Technology



http://ijtech.eng.ui.ac.id

Research Article

Photocatalytic NO_x Reduction to Ammonia Using Zirconium Incorporated g- C_3N_4 Catalyst

Desi Kurniawan¹, Wibawa Hendra Saputera^{1,2,3*}, Dwiwahju Sasongko^{1,3}

Abstract: Nitrogen oxides (NO_x) are major air pollutants that contribute to environmental and health issues. The photocatalytic reduction of NO_x into ammonia (NH_3) offers a sustainable approach to mitigating emissions while producing valuable chemical feedstocks. In this study, a zirconium-doped graphitic carbon nitride (Zr/g-C₃N₄) photocatalyst was synthesized via pyrolysis and its efficiency in NO_x reduction under visible light irradiation was evaluated. The structural, optical, and morphological properties of the photocatalyst were analyzed using X-ray diffraction (XRD), UV-Vis diffuse reflectance spectroscopy (UV-Vis DRS), scanning electron microscopy-energy dispersive X-ray (SEM-EDX), and Brunauer-Emmett-Teller (BET) surface area analysis. Zr incorporation enhanced charge separation, improved surface properties, and increased light absorption, leading to superior photocatalytic activity. Photocatalytic performance tests demonstrated that 1%Zr/g-C₃N₄ calcined at 400°C exhibited the highest ammonia yield of 119.1 $\mu g/L \cdot h \cdot g_{catalyst}$, significantly outperforming undoped g-C₃N₄. The enhanced activity was attributed to the introduction of Zr, which facilitated better electron transport and reduced photogenerated charge carrier recombination. However, excessive calcination temperatures resulted in structural degradation and photocatalytic efficiency decline. The reaction mechanism analysis confirmed that NO_x was effectively reduced to NH_3 through multi-electron transfer processes, with water oxidation occurring simultaneously to maintain charge balance. This study highlights the importance of dopant concentration and calcination conditions in optimizing photocatalytic NO_x reduction. $Zr/g-C_3N_4$ is a promising photocatalyst for environmental remediation and sustainable ammonia production, providing an innovative approach for pollution control and nitrogen cycle use.

Keywords: Ammonnia; g-C₃N₄; NO_x; Photocatalytic; Zirconium

1. Introduction

The photocatalytic reduction of nitrogen oxides (NO_x) to ammonia (NH_3) represents an innovative and environmentally sustainable strategy that supports carbon neutrality and renewable energy initiatives. This approach offers a promising alternative for mitigating GHG emissions and addressing the global energy crisis associated with fossil fuel dependence (Intergovernmental Panel on Climate Change, 2007). Photocatalysis is particularly advantageous due to its operation under mild conditions, low emission of toxic byproducts, and potential to convert harmful gas emissions, including CO_2 (Mutiara et al.,

¹Research Group on Sustainable Energy and Technology, Department of Chemical Engineering, Institut Teknologi Bandung, Bandung 40132, Indonesia

²Center for Catalysis and Reaction Engineering, Institut Teknologi Bandung, Bandung 40132, Indonesia

 $^{^3}$ Research Center for New and Renewable Energy, Institut Teknologi Bandung, Bandung 40132, Indonesia

^{*}Corresponding whsaputera@itb.ac.id, Tel.: +62-821-1768-6235

2024) (Mutiara et al., 2023), NO_x (Wahyudi et al., 2023), CH4 (Saputera et al., 2024), etc., to value-added products through integration with other technologies, such as membrane (Astuti et al., 2020).

The process is initiated when sufficient energy of light, either in the ultraviolet (UV) or visible range, excites electrons from the valence band (VB) to the conduction band (CB) of a photocatalyst, generating electron-hole pairs that drive the redox reaction (G. Li et al., 2021)(Z. Liu et al., 2021). Since NO_x mainly from combustion engines and industrial emissions, is a significant contributor to air pollution, smog, and acid rain, its conversion into NH_3 not only addresses environmental health concerns but also recovers nitrogen in a valuable form. Ammonia is widely used in fertilizers, refrigeration, and as a hydrogen carrier. Thus, it represents a strategic output aligned with sustainability and the circular economy goals.

The photogenerated electrons subsequently reduce NO_x to form ammonia, while the holes oxidize H_2O to produce oxygen (O_2) . The photocatalyst's efficiency depends largely on the separation and recombination dynamics of the photogenerated charge carriers, which ultimately influence the reaction kinetics. Ammonia gas has several advantages over hydrogen gas. It is easier to liquefy, requiring only -33°C, and needs to be compressed to just 10 times atmospheric pressure. Additionally, ammonia does not react with steel or leak from containers as hydrogen does, making it a superior carrier. Ammonia contains 50% more hydrogen by volume than hydrogen itself and converts back into hydrogen and nitrogen when needed without the intense conditions required for storing pure hydrogen gas (Whulanza et al., 2024). The application of photocatalysis using semiconductor materials is reported to be more effective than the conventional chemical oxidation methods for degradation of these pollutants (Kusdianto et al., 2019). Semiconductor materials are widely used as photocatalysts due to their electronic structures, which facilitate efficient charge separation, characterized by a high- and low-energy valence band. Among various semiconductors, graphitic carbon nitride (g-C₃N₄) has emerged as a promising candidate for NO_x reduction owing to its high reduction potential, cost-effectiveness, non-toxicity, and excellent stability. g-C₃N₄ is synthesized through the polymerization of cyanamide, dicyandiamide, or melamine, forming a polymeric structure known as melon, which consists of amino-functionalized units in a highly ordered arrangement (Henderson-Sellers, 2013).

Graphitic carbon nitride (g-C₃N₄) has emerged as a promising metal-free photocatalyst owing to its visible-light absorption (Muktaridha et al., 2021), thermal stability, and tunable electronic structure. However, its practical application in gas-phase photocatalysis, especially for NO_x reduction, is hindered by the limited surface area and rapid recombination of photogenerated charge carriers (Astuti et al., 2020). To address these limitations, the incorporation of zirconium-based compounds such as ZrO₂ into g-C₃N₄ has gained significant attention. successfully synthesized amorphous g-C₃N₄/ZrO₂ composites via one-step pyrolysis, which exhibited enhanced activity for ambient ammonia synthesis under solar light, attributed to improved charge separation and surface reactivity. Nano-ZrO₂ supported on g-C₃N₄ led to improved visible light absorption and photocatalytic degradation performance (Mou et al., 2019). Zirconium was calcined to form metal oxide (ZrO₂), which serves as an active component in the catalyst system (Rahma and Hidayat, 2023). Furthermore, the heterojunction of Zr- and N-doped TiO₂ with g-C₃N₄ nanosheets achieved efficient separation of photogenerated carriers through a Z-scheme mechanism, thereby enhancing both pollutant degradation and hydrogen evolution. Collectively, these advancements reveal that Zr-modified g-C₃N₄ systems are highly promising for selective NO_x -to- NH_3 conversion under ambient conditions (Pahi et al., 2021).

However, pure g-C₃N₄ exhibits limited charge carrier separation efficiency and restricted visible-light absorption, which hinder its photocatalytic performance. Consequently, innovative modifications, such as doping strategies, are essential for enhancing the photocatalytic capabilities of the reagent. Doping is an effective approach to improve photocatalytic efficiency and can be categorized into three types: metal doping, metal ion doping, and bimetallic doping (Zhou et al., 2021). Several strategies have been explored to enhance g-C₃N₄ performance. The first approach involves modifying the g-C₃N₄ catalyst with zirconium (Zr), while the second focuses on optimizing the NO_x pollutant conversion into ammonia. The incorporation of zirconium nitrate as a cocatalyst is one effective modification. Zirconium nitrate, with a bandgap energy (Eg) of 3,0 eV, is an economical semiconductor that effectively reduces electron-hole recombination. The integration of zirconium enhances photocatalytic activity by lowering the bandgap energy, improving UV absorption, and ultimately increasing the efficiency of ammonia production (Yi et al., 2019).

For instance, Y. Wang et al., 2023 demonstrated that Zr/g- C_3N_4 catalysts synthesized from commercial urea exhibited superior photocatalytic activity compared with pristine g- C_3N_4 . Other studies have also corroborated that Zr modification significantly enhances the photocatalytic performance. Moreover, a recent review by Gu et al., 2020 highlighted advances in g- C_3N_4 -based photocatalysts for NO_x removal, emphasizing modification strategies such as morphology control, band structure engineering, crystallinity optimization, defect engineering, and heterojunction construction to improve photocatalytic performance. Various doping strategies have been identified to enhance g- C_3N_4 photocatalytic performance in NO_x reduction. Metal and non-metal doping improve the charge separation efficiency and extend the light absorption spectra. For example, sulfurdoped g- C_3N_4 nanosheets have been investigated using density functional theory (DFT) calculations, demonstrating their potential as efficient photocatalysts for CO_2 reduction (M. Yang and Xu, 2014).

Furthermore, rare-earth and multi-element doping enhances the photocatalytic properties of g-C₃N₄. A comprehensive review has discussed the role of multi-element and rare-earth doping in g-C₃N₄ structures, including the underlying mechanisms and their impact on photocatalytic performance. Another promising strategy involves the incorporation of metal oxides such as ZnO into Mo-doped g-C₃N₄, which has exhibited improved photodegradation activity for organic pollutants such as MB and RhB. Collectively, these modification strategies contribute to the enhancement of g-C₃N₄ photocatalytic efficiency in environmental applications, particularly in NO_x reduction to ammonia (Q. Yu and Brouwers, 2009). Ammonia (NH₃) produced from the photocatalytic NO_x reduction was detected using the Indophenol blue method due to its high sensitivity and selectivity. In this method, NH₃ reacts with phenol and hypochlorite under alkaline conditions to form a blue complex, which is quantified using UV-Vis spectrophotometry at 640 nm. This method is widely used because it is simple, cost-effective, and reliable, with minimal interference from other nitrogen species.

In this study, g-C₃N₄ photocatalysts were synthesized via pyrolysis and modified with Zr as a cocatalyst to form Zr/g-C₃N₄ at various calcination temperatures (400°C, 500°C, and 600°C). The efficiency of the photocatalysts in reducing NO_x to ammonia under irradiation from a 300 W xenon lamp was then evaluated. The synthesized photocatalysts were comprehensively characterized using various analytical techniques, including X-ray diffraction (XRD), UV-Vis diffuse reflectance spectroscopy (UV-Vis DRS), and surface area and porosity analysis. These characterizations provide critical insights into the structural, optical, and surface properties of the catalysts, thereby contributing to a deeper

understanding of their photocatalytic behavior and potential applications in sustainable environmental remediation.

2. Materials and Methods

2.1 Materials

Zirconium nitrate $(Zr(NO_3)_4, 99.7\%)$ was purchased from Jinan Future Chemical Co., Ltd., China. Urea ([(NH₂)₂.CO], 99%), ethanol (C₂H₆O, 95%), sodium nitrate ([Na(NO₃)₄], 99.5%), and trisodium citrate dihydrate (C₆H₈O₇Na₃.2H₂O) were purchased from Merck Chemicals and Life Sciences. All chemicals used in this process were analytical grade and not further purified.

2.2 Synthesis of graphite carbon nitride

The graphitic carbon nitride photocatalyst was synthesized using the pyrolysis (thermochemical) method, as shown in Figure S1. Briefly, 10 g of urea was dissolved in 10 ml of ethanol and then some amount of zirconium nitrate was added according to the molar percent variation with magnetic stirring for several minutes. Then, it was poured into a Petri dish to evaporate ethanol into air for 6-8 hours. Finally, the powders were collected and placed in a lidded quartz crucible and heated in a muffle furnace with temperature variations of 400°C, 500°C, and 600°C for 3 h. The synthesized samples were labeled as x Zr-C-y (x refers to the molar percentage of Zr and y represents the calcination temperature).

2.3 Characterization of GC nitride

XRD analysis was performed using a Bruker D2 Phaser (Bruker Corporation, Billerica, MA, USA) to investigate the crystal structure of g-C₃N₄-based photocatalysts. The crystallite size was calculated using the Scherrer equation, as shown in Equation (1). Here, (D) is the crystallite size (nm), (K) is the shape factor, (λ) is the X-ray wavelength (e.g., 1.5406 Å for Cu K α), (β) is the FWHM in radians, and (θ) is the Bragg angle (in radians). The degree of crystallinity was determined using Equation (2), where (X_c) is the degree of crystallinity (in percentage), (A_c) is the area under the crystalline peaks, and ($A_{\rm total}$) is the total area under the XRD curve, including both crystalline and amorphous contributions.

$$D = \frac{K}{\beta cos\theta} \tag{1}$$

$$X_c = \frac{A_c}{A_{total}} \times 100\% \tag{2}$$

The NOVA 2200e Surface Area & Pore Size Analyzer (Quantachrome Instruments, Boynton Beach, FL, USA) was used to evaluate the specific surface area, pore volume, and pore size distribution. The specific surface area was determined using the Brunauer–Emmett–Teller (BET) method, while porosity parameters were analyzed using the BJH method. Diffuse reflectance spectra were recorded in the wavelength range of 200–800 nm using a UV-Vis spectrophotometer (Shimadzu UV-2600i, Japan) and converted to absorbance via the Kubelka–Munk method to determine the band gap of the

photocatalyst, with BaSO₄3 as the reference material. Additionally, the catalyst morphology was examined using a scanning electron microscope equipped with energy-dispersive X-ray spectroscopy (SEM-EDX, Hitachi High Technologies SU3500, Tokyo, Japan).

2.4 Photocatalytic Assessment of NO_X to Ammonia Reaction

The photocatalytic reduction of NO_X to ammonia was carried out in a 500 mL cylindrical flask reactor using a 300 W xenon lamp as the light source. The photocatalyst (0.36 g) was dispersed into 300 mL of 300 ppm of NaNO₃ solution and stirred with a magnetic stirrer at 350 rpm until homogeneous. Then, N_2 gas was added to the solution for 30 min to eliminate dissolved gases, ensuring the removal of oxygen. Then, the xenon lamp was turned on, and the photocatalytic reaction occurred. A 3 mL solution was collected every 5 min using a syringe for spectrophotometric analysis. This study examined the influence of various photocatalyst synthesis parameters, including reaction time (0.5–2 h), molar ratio, and calcination temperature. Additionally, the impact of zirconium precursor concentration (0.1%, 0.5%, and 1%) on g-C₃N₄ calcined at 400°C, 500°C, and 600°C was evaluated. Selected samples, produced under optimized reaction conditions, were further analyzed for data comparison using UV-Vis Spectrophotometry (Shimadzu UV 2600i, Japan). The molar ratio and reaction time were optimized to maximize the yield of ammonia.

2.5 Ammonia yield analysis

The liquid sample was analyzed using the indophenol blue method, followed by UV-VIS double-beam spectrophotometry. This method required the preparation of several reagents. The sodium citrate solution was prepared by dissolving 400 g of trisodium citrate dihydrate in deionized water to a final volume of 1 L. The phenol solution was prepared by dissolving 2 g of sodium hydroxide and 4 g of phenol in distilled water to a final volume of 100 mL. The sodium hypochlorite solution was prepared by diluting 4 mL of commercial sodium hypochlorite in distilled water to a final volume of 100 mL. The sodium nitroprusside solution was prepared by dissolving 0.05 g of sodium nitroprusside in 100 mL of 3 N sodium hydroxide solution.

Before conducting the sample analysis, a concentration-absorbance calibration curve was established using NH4Cl standard solution with NH₃ concentrations of 0.0, 0.5, 1.0, 1.5, 2.0, 2.5, and 3.0 ppi in a 0.1 M HCl solution. The indophenol blue method was performed by transferring a 5 mL water sample into a 10 mL Erlenmeyer flask, followed by the sequential addition of 1 mL of sodium citrate solution, 0.1 mL of phenol solution, and 0.05 mL of sodium hypochlorite solution, with continuous stirring after each addition. After 5 min, 0.1 mL of sodium nitroprusside solution was added to accelerate indophenol blue formation. The sample was then sealed with parafilm and incubated in the dark at room temperature for at least 1 h. Finally, the absorbance was measured at wavelengths of 420 and 620 nm using UV-vis spectrophotometry (Shimadzu UV 2600i, Japan).

3. Results and Discussion

3.1 Characterization of GC nitride

XRD characterization was conducted to analyze the crystallinity and crystal structure of the catalyst. $\rm Zr/g\text{-}C_3N_4$ photocatalysts were synthesized at 400°C, 500°C and 600°C, to evaluate the effect of temperature on crystallinity, examine structural changes resulting from precursor variations, and determine the degree of crystallinity and crystallite size,

as shown in Figure 1. Based on Figure 1a, The dominant diffraction peak observed at approximately 2θ of 27.4° corresponds to the interlayer stacking of the g-C₃N₄ structure, with a d-spacing of 0.326 nm. Additionally, a weaker peak at around 2θ of 13.1° represents the in-plane arrangement of the melamine (hexagonal) units, identifying the structural features of the materials (X. Zhang et al., 2018)(L. Zhang et al., 2019).

The incorporation of metal precursors, such as zirconium (Zr), can alter the structural, electronic, and photocatalytic properties of $g_{-3}N_4$. Zirconium is commonly used to enhance catalytic activity by modifying the crystal structure, introducing defects, and improving the optoelectronic properties. It can be incorporated into $g_-C_3N_4$ via doping or composite formation. During doping, Zr^{4+} ions can substitute carbon or nitrogen atoms within the $g_-C_3N_4$ framework, generating structural defects that enhance catalytic reactivity (Gu et al., 2020). XRD analysis of zirconium-doped $g_-C_3N_4$ reveals shifts in peak intensity and position, particularly at 2θ of 26.74° and 12.46° when calcined at 400°C (Figure 1b).

The effect of the concentration of the zirconium precursor (0.1%, 0.5%, and 1%) on g-C₃N₄ was evaluated at calcination temperatures of 400°C, 500°C, and 600°C, as shown in Figure 1b-1d. At a 0.1% zirconium concentration, minimal structural defects were observed in the g-C₃N₄ framework, with the dominant diffraction peak remaining at 2θ of 27.22°. At 0.3% zirconium concentration, a slight shift toward a lower 2θ angle was detected, indicating an increase in interlayer spacing (d-spacing) due to the incorporation of Zr⁴⁺ ions.

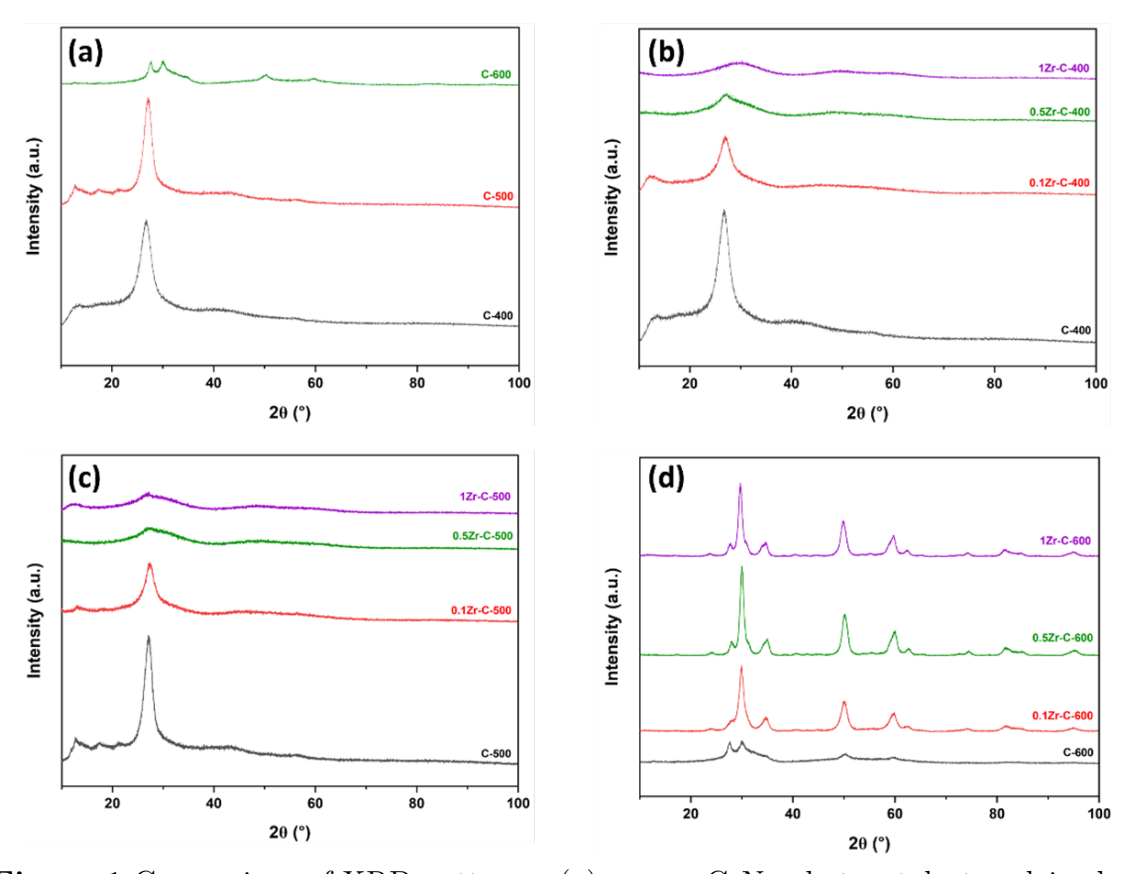


Figure 1 Comparison of XRD patterns: (a) pure g-C₃N₄ photocatalysts calcined at 400° C, 500° C, and 600° C, (b) Zr-modified g-C₃N₄ calcined at 400° C, (c) Zr-modified g-C₃N₄ calcined at 500° C, and (d) Zr-modified g-C₃N₄ calcined at 600° C

The peak intensity decreased significantly at 0.5% zirconium concentration, indicating greater disruption in the layered structure. Additional weak diffraction peaks were

observed, indicating the possible formation of new phases or increased porosity. However, at 1% zirconium concentration, the main peak weakened considerably or even merged, signifying severe disruption of the graphitic structure. New amorphous or crystalline phases derived from zirconium compounds were formed.

Table 1 reveal that both the calcination temperature and Zr doping concentration significantly influence the crystallite structure and layer arrangement of g-C₃N₄. An increase in the calcination temperature from 400°C to 600°C generally leads to a higher crystallite size and number of stacking layers, indicating improved crystallinity. However, Zr incorporation modifies this trend depending on the doping level. For instance, 0.10Zr-C-600 exhibits an anomalously low 2θ value (24.110°) and a larger interlayer distance (d = 0.332nm), indicating structural distortion or exfoliation effects at elevated temperatures. At moderate Zr loading (0.10 and 0.50 wt%), there is a slight increase in the crystallite size and layer stacking with temperature, but at high Zr content (1.0 wt%), the crystallinity appears to be suppressed, especially in 1.0Zr-C-400 and 1.0Zr-C-500 samples, where the crystallite size remains small (5.5–6.6nm) despite increasing calcination temperature. Excessive Zr doping may hinder crystal growth and introduce defects or distortion in the g-C₃N₄ lattice.

To evaluate the bandgap and optical properties of the synthesized photocatalyst, a UV-Vis DRS analysis was conducted. Figure 2 shows the absorbance and Kubelka-Munk spectrum analysis of $\rm Zr/g\text{-}C_3N_4$ catalysts at various Zr ratios and calcination temperatures.

Figure 2a illustrates the absorbance spectra at 400°C, with wavelength (nm) on the Xaxis and absorbance (a.u) on the Y-axis, representing material combinations synthesized under different zirconium ratios and calcination temperatures. Absorbance peaks are observed around 315-320 nm, indicating variations in light interaction due to composition and thermal treatment. (M. Yang and Xu, 2014). The g-C₃N₄ photocatalyst exhibits a peak at 316 nm, absorbing more light than other samples, indicating its potential to capture a larger portion of the solar spectrum, enhance charge carrier separation, reduce recombination rates, and lower energy consumption costs. In Figure 2c, the absorbance spectrum at 500°C shows a shift within the 300–337 nm range, with the 0.3Zr/g-C₃N₄ photocatalyst peaking at approximately 337 nm, indicating enhanced light absorption due to Zr doping and its impact on the material's electronic structure and surface properties (Q. Yu and Brouwers, 2009). Meanwhile, Figure 2e presents the absorbance spectrum at 600°C, revealing a peak at 311 nm, with shifts in absorption wavelengths influenced by calcination temperature, Zr doping concentration, and synthesis conditions. These findings highlight how controlled synthesis parameters affect the optical properties of Zr/g-C₃N₄, emphasizing the role of thermal and compositional modifications in optimizing the performance of the photocatalyst.

The UV-Vis DRS analysis, using the Kubelka-Munk method, determines the bandgap energy (Eg) of the material using the Tauc plot approach. As shown in Figure 2b, the bandgap energy ranges from 2.63 to 3.23 eV at 400°C, indicating semiconductor properties. The absorption band at 316 nm corresponds to an electronic transition from the valence to the CB. Figure 2d shows a bandgap range of 2.62–3.27 eV at 500°C, with higher zirconium doping leading to increased bandgap values. In contrast, Figure 3f at 600°C shows a significant rise in bandgap energy (4.20–4.96 eV), indicating that the calcination temperature strongly influences the bandgap. Generally, higher temperatures reduce the bandgap due to energy band broadening from thermal vibrations, enhancing the electrical conductivity. The structure can be tailored through doping, synthesis techniques, temperature, pressure, and precursor ratios. Similar to graphene, g-C₃N₄ has a layered

2D structure that is held together by van der Waals forces and $\pi - \pi$ interactions. It consists of sp²-hybridized carbon and nitrogen, with σ bonds forming aromatic rings and conjugated sheets. The valence band is composed of N(pz) orbitals, while the conduction band consists of C(pz) orbitals, enabling light absorption in the visible range ($\lambda < 460$ nm) (Nosaka and Nosaka, 2017).

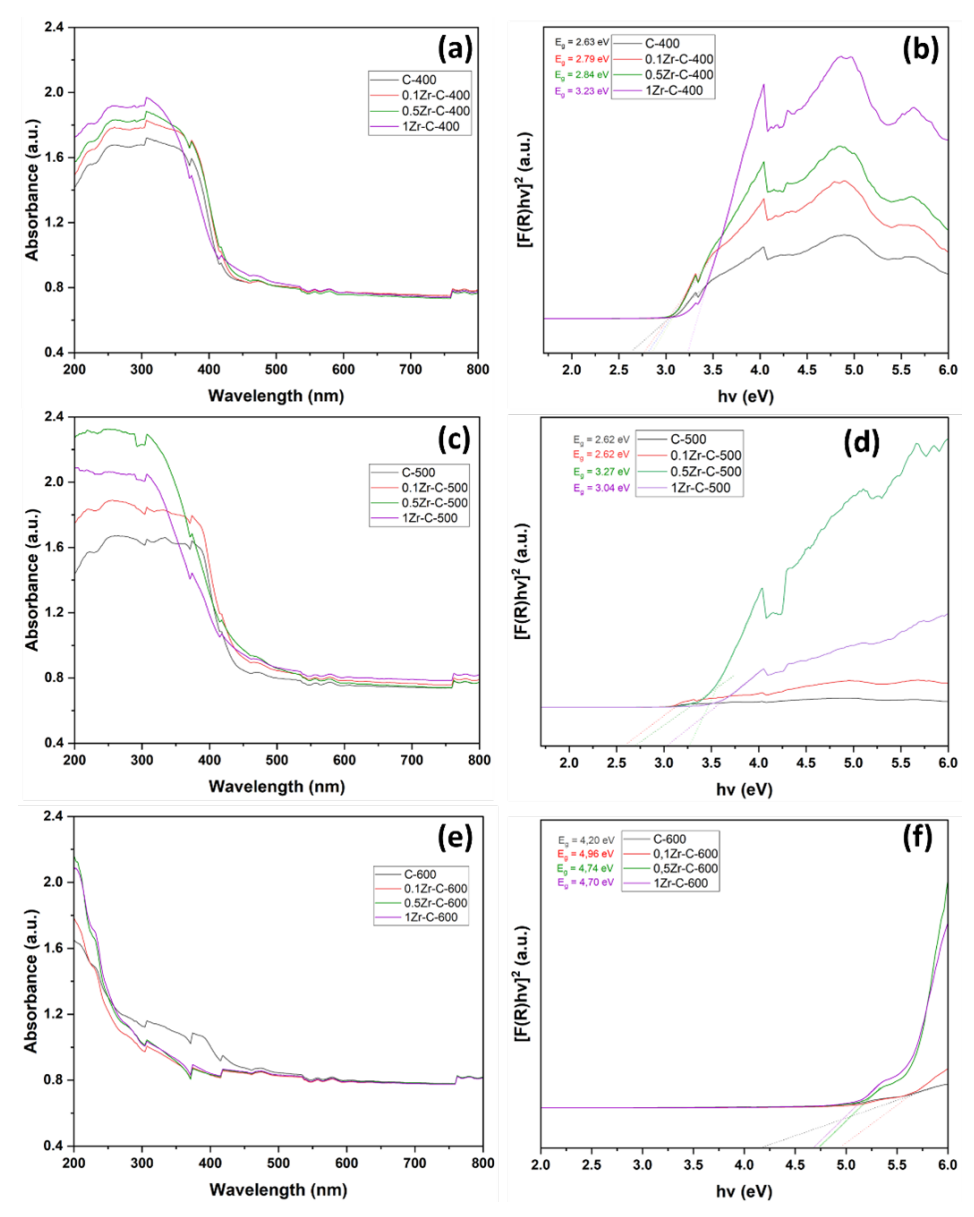


Figure 2 UV-Vis diffuse reflectance spectroscopy (DRS) and Tauc plot analysis of Zr/g-C₃N₄ photocatalysts. (a, c, e) UV-Vis absorbance spectra of photocatalysts calcined at 400°C, 500°C, and 600°C. (b, d, f) Corresponding Tauc plots used to determine the bandgap energies of the photocatalysts at 400°C, 500°C, and 600°C

In addition, by combining surface area, pore structure, and nitrogen physisorption analysis, the impact of calcination temperature and Zr loading on textural properties was revealed. As shown in Table 1, pure g-C₃N₄ photocatalysts exhibit variations in surface area, pore volume, and pore size depending on calcination temperature. Among them, C-500 demonstrates the highest surface area (58.73 m²/g) and pore volume (0.1341 cm³/g), while C-600, despite a slightly lower surface area (56.03 m²/g), exhibits a much larger average pore radius (5.17 nm), indicating the development of a mesoporous structure. Significant modifications in textural properties are observed upon Zr incorporation.

Tabel 1 Summary of band gap determination, surface area, pore characteristic, and crystallite size measurement of $\rm Zr/g\text{-}C_3N_4$ photocatalysts with various Zr loading and calcination synthesis temperature

No.	Photocatalyst	Bandgap	Surface	Pore	Average	Crystallite
		value (eV)	area (m^2/g)	volume	pore radius	Size
				(cm^3/g)	(nm)	
1	C-400	2.63	17.4	0.033	1.61	6.5
2	C-500	2.62	58.7	0.134	1.61	7.8
3	C-600	4.20	56.0	0.120	5.17	9.1
4	$0.10 \mathrm{Zr}\text{-}\mathrm{C}\text{-}400$	2.79	16.1	0.034	1.61	6.0
5	$0.10 \mathrm{Zr}\text{-}\mathrm{C}\text{-}500$	2.62	63.8	0.168	9.09	7.1
6	$0.10 \mathrm{Zr}\text{-}\mathrm{C}\text{-}600$	4.96	34.9	0.091	6.61	8.6
7	$0.50 \mathrm{Zr}\text{-}\mathrm{C}\text{-}400$	2.84	18.9	0.048	9.06	5.8
8	$0.50 \mathrm{Zr}\text{-}\mathrm{C}\text{-}500$	3.27	68.6	0.191	8.99	6.9
9	$0.50 \mathrm{Zr}\text{-}\mathrm{C}\text{-}600$	4.74	47.6	0.106	1.77	8.3
10	1.0 Zr-C- 400	3.23	31.4	0.064	1.61	5.5
11	1.0 Zr-C-500	3.04	21.1	0.059	6.63	6.6
12	$1.0 \mathrm{Zr}\text{-}C\text{-}600$	4.70	49.5	0.099	1.60	7.5

Moderate Zr loading, such as 0.50Zr-C-500, enhances the surface area $(68.58 \text{ m}^2/\text{g})$ and pore volume $(0.1913 \text{ cm}^3/\text{g})$, indicating improved porosity. However, excessive Zr incorporation, such as in 1.0Zr-C-500, leads to a drastic reduction in the surface area $(21.10 \text{ m}^2/\text{g})$ and pore volume $(0.0587 \text{ cm}^3/\text{g})$, likely due to pore blockage or structural changes. These trends are further supported by the nitrogen physisorption isotherms shown in Figure S2.

SEM was employed to analyze the surface morphology and microstructure of graphitic carbon nitride (g-C₃N₄). Figure 3 illustrates the morphological characteristics of the synthesized g-C₃N₄-based photocatalysts, revealing the effects of Zr modification and calcination temperatures. The pure g-C₃N₄ sample (C-400) exhibited a characteristic layered and sheet-like structure with visible agglomeration (Figures 3a and 3b), which may have influenced its surface area and catalytic activity. Upon zirconium incorporation at 0.1 wt% (0.1Zr-C-400), the material shows increased roughness and compact clustering (Figure 3c), indicating the formation of additional active sites that could enhance the photocatalytic performance. Further increasing the zirconium content to 1 wt% (1Zr-C-400) results in more pronounced NP aggregation and a rougher (Figure 3d), more porous surface, indicating a higher surface area that may improve light absorption and charge separation.

As the calcination temperature increased to 500°C (1Zr-C-500), the material became denser, with more compact clustering and a somewhat heterogeneous particle distribution (Figure 3e), which might have reduced the number of accessible active sites. At 600°C (1Zr-C-600), the structure appears highly aggregated and disordered (Figure 3f), with signs of sintering that may lead to a loss of surface porosity, potentially decreasing its catalytic efficiency (Paul et al., 2019). Overall, Zr modification enhances surface roughness and active site distribution, whereas higher calcination temperatures tend to induce densification and aggregation. Among the tested samples, 1Zr-C-400 appears to have the most favorable morphology, balancing porosity and surface texture, making it a promising candidate for enhanced photocatalytic activity.

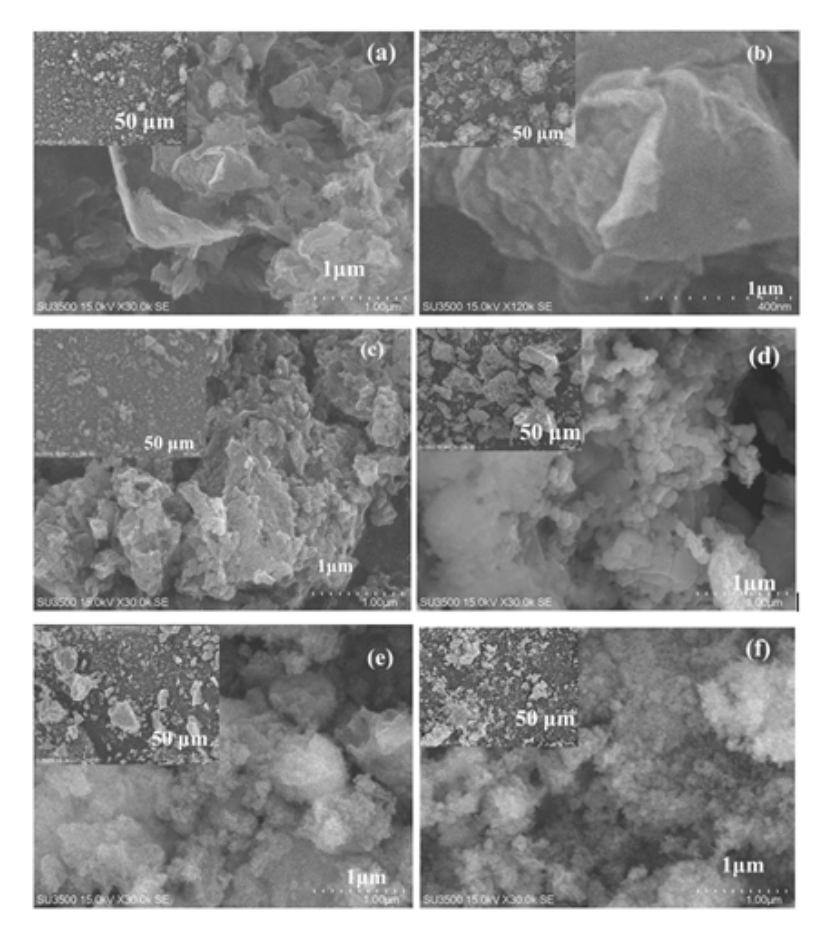


Figure 3 SEM images of the Zr/g-C₃N₄ photocatalysts. (a, b) C-400, (c) 0.1Zr-C-400, (d) 1Zr-C-400, (e) 1Zr-C-500, and (f) 1Zr-C-600. Insets show lower magnification images at 50 μ m scale

The particle sizes of the graphitic carbon nitride (g- C_3N_4) photocatalysts have been estimated based on SEM analysis. The pristine g- C_3N_4 sample (C-400) exhibited particle sizes ranging from 120 to 150 nm. Upon the introduction of zirconium (Zr) at a molar ratio of 1% and calcination at 400°C, the particle size decreased significantly to 70–95 nm for the 1Zr-C-400 sample. This reduction is attributed to the Zr species inhibiting the agglomeration of g- C_3N_4 during thermal treatment, thereby promoting smaller and more dispersed particles. When the calcination temperature was increased to 500°C (1Zr-C-500), the particle size slightly increased to 80–100 nm, likely due to moderate sintering effects. Further increasing the temperature to 600°C (1Zr-C-600) led to a more noticeable growth in particle size (100–130 nm), which can be attributed to enhanced crystallite coalescence and thermally induced grain growth. These trends indicate that Zr incorporation contributes to improved control over particle morphology at lower temperatures, while excessive calcination may reverse this benefit due to thermal aggregation.

Generally, the layered structure of g- C_3N_4 typically consists of stacked thin sheets, resembling graphite. Particle size and aggregation occur due to van der Waals forces between layers, forming irregular clusters. Some samples exhibit porous structures, which are crucial for photocatalytic and adsorption applications. Doping-induced morphological changes were also evident. The structure consists of ultrafine fibers with strip-like pores between the fibers at low doping concentrations. The morphology transforms into porous sheets resembling thick fibers as the doping concentration increases, but the strip-like porous structure diminishes (L. Zhang et al., 2019).

Figure S3 presents the SEM-EDX mapping results of the 1Zr-C-400 photocatalyst.

The morphology appears as agglomerated sheets with a rough and porous surface (Figure S3a). The Zr metal was more evenly dispersed across the photocatalyst surface (Figure S3b). Furthermore, the 1Zr-C-400 photocatalyst is primarily composed of C, N, and Zr elements, as shown in Figures S3c and S3d.

3.2 Photocatalytic Study on the Reduction of NO_x to Ammonia

Calcination temperature and zirconium (Zr) doping significantly influence the photocatalytic conversion of nitrogen oxides (NO_x) to ammonia (NH_3) using g- C_3N_4 . Figure 4a illustrates that among the unmodified g-C₃N₄ samples, the catalyst calcined at 500°C (C-500) exhibited the highest ammonia yield of 24.5 μ g/Lhg, outperforming those calcined at 400°C (17.7 μ g/Lhg catalyst) and 600°C (6.7 μ g/Lhg catalyst). This indicates that 500°C is the optimal calcination temperature for forming a well-ordered graphitic structure, which enhances photocatalytic efficiency due to improved crystallinity and surface area. In contrast, a higher calcination temperature (600°C) leads to structural degradation, reducing the number of active sites and limiting the efficiency (Qu et al., 2016). This structural transformation is supported by XRD analysis, where the diffraction peaks remain weak at 400°C (Figure 1b), indicating a poorly structured graphitic phase. As the temperature increased to 500°C (Figure 1c), the peaks became sharper and more intense, signifying a more ordered graphitic structure, which enhanced the charge separation and NO_r adsorption. However, the peaks weakened at 600°C (Figure 1d), indicating thermal decomposition and the formation of an amorphous carbon phase, which negatively affects the photocatalytic activity.

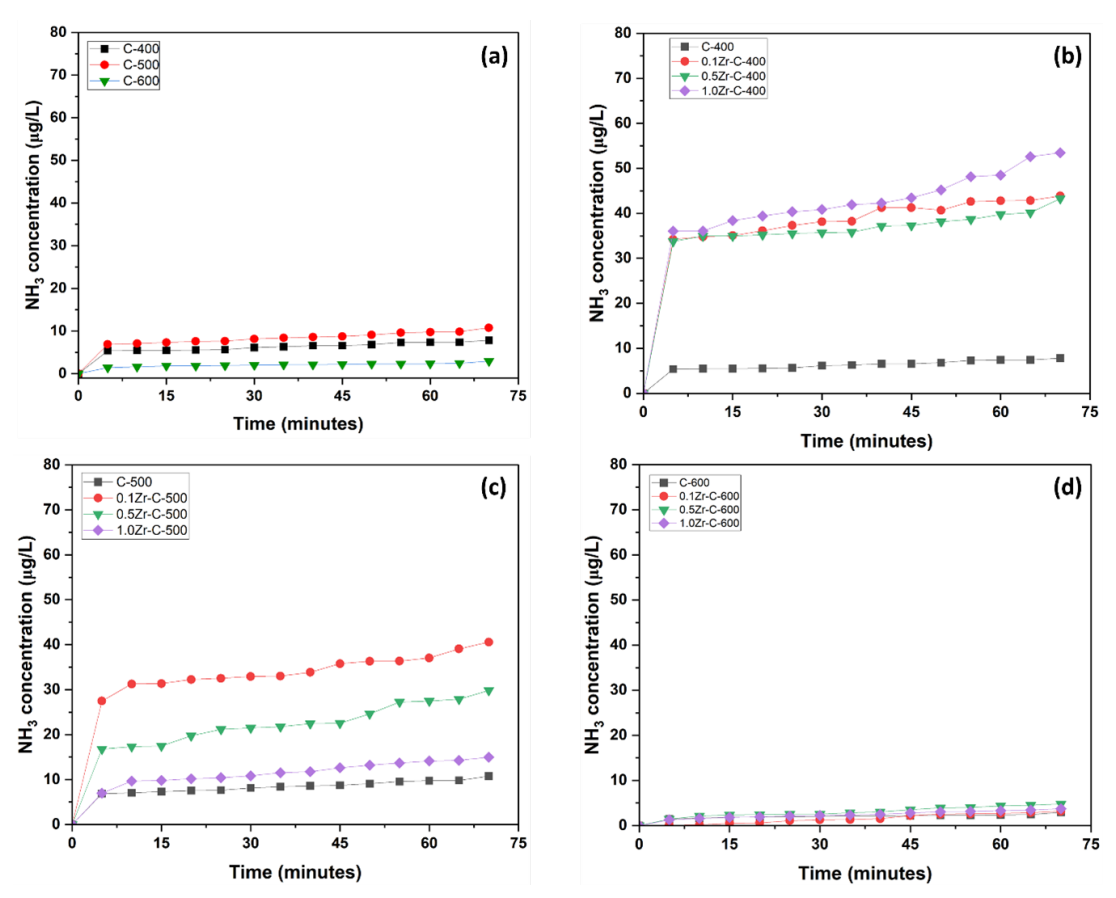


Figure 4 NO_X photocatalytic activity test results using a) Unmodified g-C₃N₄ photocatalyst at 400°C, 500°C and 600°C (b) $\rm Zr/g$ -C₃N₄ photocatalyst at 400°C (c) $\rm Zr/g$ -C₃N₄ photocatalyst at 500°C (d) $\rm Zr/g$ -C₃N₄ photocatalyst at 600°C

Zirconium doping further modifies the photocatalytic performance, as shown in Figures 4b–d, where Zr/g- C_3N_4 catalysts exhibit enhanced NH₃ production compared with their unmodified counterparts. At 400°C (Figure 4b), 1%Zr/g- C_3N_4 -400 achieves the highest ammonia yield of 119.1 μ g/Lhg catalyst, significantly surpassing undoped g- C_3N_4 . This trend depicts that increasing Zr doping improves ammonia production by increasing the number of active sites and enhancing the charge transfer efficiency. The incorporation of Zr facilitates the formation of porous structures, which improves electron mobility and reduces recombination rates. Additionally, g- C_3N_4 has been reported to exhibit high NO removal efficiency due to its electronic structure and active sites, and Zr doping likely enhances this effect by improving the interconnected nanosheet structure and charge separation efficiency (M. Yu et al., 2025; Mariyappillai et al., 2025).

However, at 500°C (Figure 4c), Zr doping led to a lower NH₃ yield compared to at 400°C, with 0.1%Zr/g-C₃N₄-500 recording the highest ammonia yield of 94.7 μ g/Lhg catalyst. This may be attributed to the structural stabilization of the C=N and C-N bonds, which enhances NO_x adsorption and provides active sites for photocatalytic reactions. Nevertheless, electron-hole recombination still poses a challenge at this temperature, limiting the overall photocatalytic efficiency. (Khan et al., 2015).

At 600°C (Figure 4d), the photocatalytic efficiency declines significantly, with the highest NH₃ yield recorded at only 12.1 μ g/Lhg catalyst for 0.5%Zr/g-C₃N₄-600. This decrease is attributed to thermal decomposition, reduced surface area, and loss of active sites. Additionally, at high temperatures, Zr particles tend to agglomerate, increasing particle size and reducing doping efficiency, thereby weakening the interaction between Zr and g-C₃N₄. Elevated calcination temperature also enhances electron-hole recombination, further diminishing the photocatalytic activity. (Khanal et al., 2021).

Figure 5 summarizes the ammonia yield after 1 h of photocatalytic testing, demonstrating the combined effects of calcination temperature and Zr doping. Among the undoped g-C₃N₄ samples, g-C₃N₄-500 exhibited the highest NH₃ yield (24.5 μ g/Lhg catalyst), followed by C-400 and C-600, confirming that 500°C is the most effective calcination temperature. The enhanced performance of C-500 can be attributed to the increased surface area and optimized visible light absorption, which result from the controlled thermal decomposition of nitrogen-rich precursors at this temperature. (Fidan et al., 2021). For Zr-doped g-C₃N₄ at 400°C (Figure 8, left panel), 1%Zr/g-C₃N₄-400 exhibited the highest NH₃ yield (119.1 μ g/Lhg catalyst), highlighting the beneficial role of Zr doping in enhancing photocatalytic performance. This enhancement is likely due to the introduction of additional porous structures and improved charge separation, which promotes NO_x adsorption and reduction. At 500°C (Figure 7, middle panel), the Zr-doped catalysts outperformed the undoped g-C₃N₄, with 0.1%Zr/g-C₃N₄-500 achieving the highest yield (94.7 μ g/Lhg catalyst). Stabilization of the tri-s-triazine structure at this temperature improves NO_x adsorption and provides active sites for reduction reactions.

However, the electron-hole recombination rate remains relatively high, limiting further improvement in the yield of ammonia (L. Zhang et al., 2019). In contrast, at 600°C (Figure 5, right panel), ammonia yields drop significantly, with the highest value of only $12.1~\mu g/Lhg$ catalyst observed for $0.5\%Zr/g-C_3N_4-600$. The decline in performance can be attributed to structural degradation, reduced surface area, and Zr particle agglomeration, which negatively impact the photocatalytic process. (H. Li et al., 2023; Sun et al., 2023; Y. Wang et al., 2023; Mutiara et al., 2023; Wahyudi et al., 2023; Zhanyong et al., 2023). The results confirm that the combination of appropriate Zr doping and calcination temperature is critical for optimizing the photocatalytic performance of g-C₃N₄. The findings align with the literature, which indicates that moderate doping enhances charge

separation and reaction kinetics, whereas excessive calcination or doping can degrade photocatalyst efficiency due to structural damage and increased recombination rates (Qu et al., 2016).

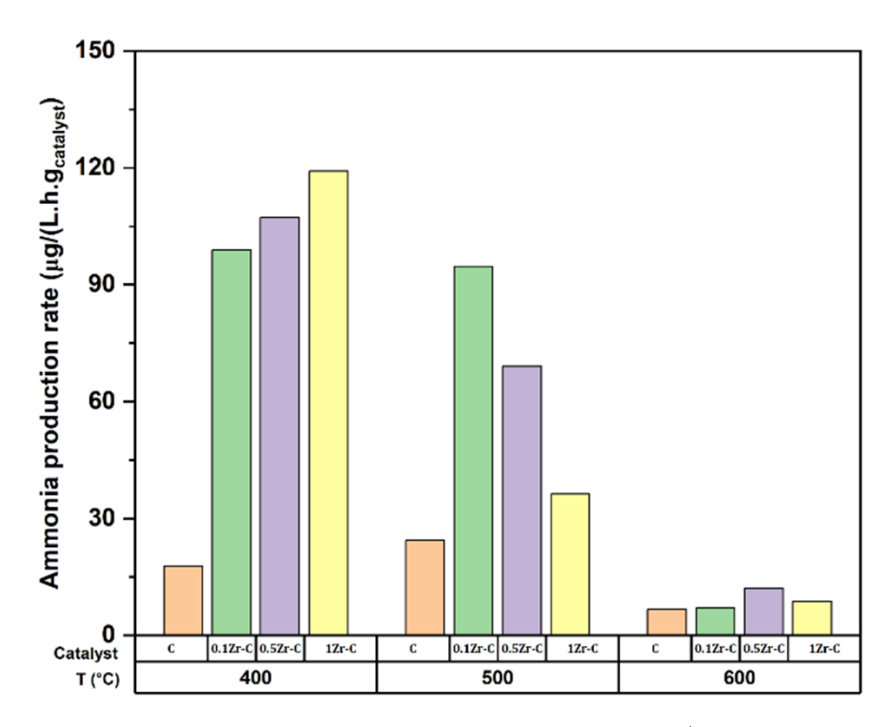


Figure 5 Ammonia production rate over different catalysts (C, 0.1Zr–C, 0.5Zr–C, and 1Zr–C) at various reaction temperatures (400°C, 500°C, and 600°C) after 1h photocatalytic activity testing

3.3 Photocatalytic reaction mechanism of NO_x to ammonia with $Zr/g-C_3N_4$ photocatalysts

Figure 6 illustrates the photocatalytic reduction of NO_x to NH_3 using $Zr/g-C_3N_4$ as a semiconductor photocatalyst, highlighting the reaction mechanism and the role of Zr doping in enhancing the photocatalytic performance. Upon light irradiation $(h\nu)$, g- C_3N_4 generates electron-hole pairs, where excited electrons migrate to the conduction band (CB) while holes remain in the VB. These charge carriers participate in redox reactions that drive the conversion of NO_x into NH_3 . Specifically, NO reacts with H^+ and photogenerated electrons to form NH_3 and H_2O , while NO_2 undergoes a similar reduction process requiring additional protons and electrons, producing NH_3 and excess water. Water oxidation occurs in the valence band, where holes facilitate the generation of O_2 and H^+ ions, contributing to the NO_x reduction reaction.

The schematic also emphasizes the effect of Zr doping, which significantly improves the photocatalytic efficiency. Zr incorporation into $g-C_3N_4$ enhances charge separation by minimizing electron-hole recombination, thereby increasing the number of available electrons for NO_x reduction. Additionally, Zr-modified $g-C_3N_4$ exhibits improved electron transfer efficiency, ensuring a more effective conversion of NO_x to NH_3 . Structurally, Zr doping introduces defect sites, slightly altering the electronic structure and optimizing the catalytic activity of $g-C_3N_4$. The modified photocatalyst demonstrates superior performance in NO_x reduction compared to undoped $g-C_3N_4$. The series of reactions is illustrated in Equations (1)–(4) as follows:

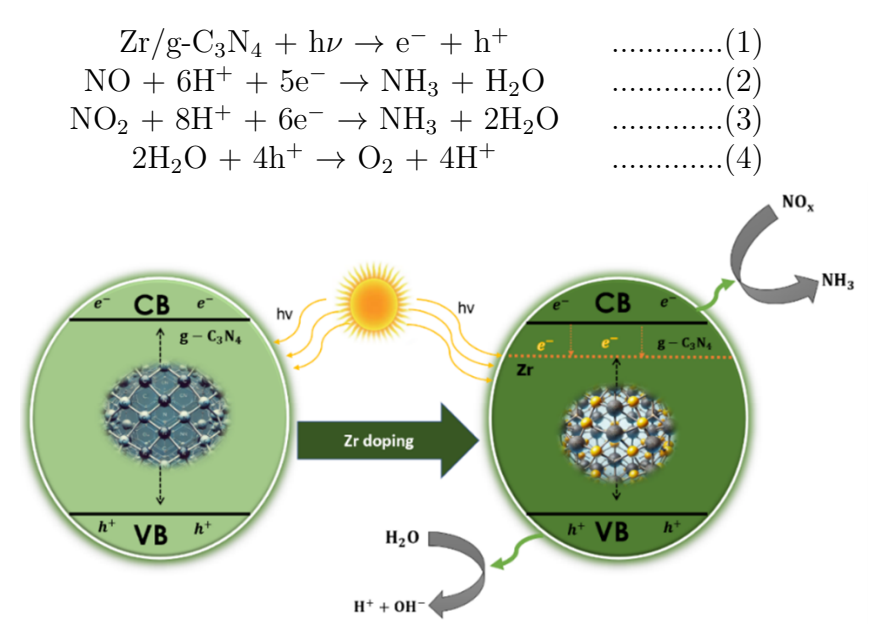


Figure 6 Schematic illustration of photocatalytic NOx reduction to ammonia using $Zr/g-C_3N_4$ photocatalyst semiconductor

The formation of ammonia (NH₃) observed during the photocatalytic reduction of NO_x is a surface-mediated process that can be effectively interpreted using the modified Langmuir-Hinshelwood (L-H) kinetic model. This model assumes that the reaction rate depends on the surface coverage of adsorbed reactants and incorporates both adsorption equilibrium and surface reaction kinetics. According to the L-H framework, the rate of NH₃ production is governed by the equation $r = \frac{kKC}{1+KC}$, where r is the reaction rate, k is the intrinsic rate constant, K is the adsorption equilibrium constant, and C is the NO_x concentration. This approach has been widely adopted to describe gas-phase photocatalytic reactions on semiconductor surfaces, including NO_x removal and nitrogen species conversion (H. Yang et al., 2019; X. Li et al., 2020). The application of this model allows for quantifying the influence of doping elements—such as zirconium—on both adsorption affinity and surface reactivity. Previous studies have shown that dopants can modify the electronic structure and active sites of g-C₃N₄, thus influencing the rate constants and shifting the reaction pathway toward selective NH₃ formation (J. Zhang et al., 2014). Further kinetic fitting using experimental NH₃ production data is essential to extract accurate parameters and verify the model's applicability under atmospheric pressure photocatalytic conditions.

Table 2 compares ammonia recovery from various g-C₃N₄-based photocatalysts, high-lighting differences in catalyst composition, dosage, operating conditions, ammonia detection methods, and recovery rates. The Zr/g-C₃N₄ photocatalyst developed in this study achieved an ammonia recovery of 119.1 μ g/Lhg, making it one of the most efficient photocatalysts tested. This high performance was obtained under 300 W Xenon lamp irradiation ($\lambda \geq 420$ nm) using the indophenol blue method for ammonia detection. The significant increase in ammonia production compared to bare g-C₃N₄ (93.1 μ g/Lhg catalyst) indicates that Zr doping enhances photocatalytic activity by improving charge separation and introducing more active sites. The choice of the ammonia detection method also influenced the recovery rates reported. The indophenol blue method was primarily used for high-performance catalysts to ensure sensitive and accurate quantification of ammonia. Meanwhile, Nessler reagent was mainly applied to catalysts with lower ammonia yields, and ion chromatography was used for composites such as g-C₃N₄/TiO₂

 $(78.6 \ \mu g/(L \cdot h \cdot gcatalyst))$. These differences highlight the importance of standardizing detection techniques when comparing photocatalyst performance. The Zr/g-C₃N₄ photocatalyst in this study demonstrated a higher ammonia production rate than undoped g-C₃N₄ and most composite materials, although B-g-C₃N₄ exhibited the highest performance. The results confirm that metal doping plays a critical role in enhancing the photocatalytic efficiency of g-C₃N₄ for NO_x reduction and ammonia synthesis applications, emphasizing the need for further optimization of dopant selection and reaction conditions.

Tabel 2 Comparison of ammonia production rates from NO_X reduction using different photocatalysts. The table lists photocatalyst type, dosage, light source, detection method, and ammonia yield, highlighting the performance of $Zr/g-C_3N_4$ from this study against previously reported materials

No.	Photocatalyst	Dosage	Operating conditions	Ammonia detection	Ammonia production	Reference
			Conditions	method	rate	
				memod	$(\mu g/L.h.g_{cataly})$,)
1	$ m Zr/g$ - $ m C_3N_4$	0.36 g	300 W	Indophenol	119.1	$\frac{st}{}$ This study
_	21/8 03114	0.00 8	Xenon lamp	blue	110.1	This study
2	B - g - C_3N_4	$0.15 \; {\rm g}$	300 W	Nessler	313.9	(X. Li et al.,
	_ 0 00-14	31-3 8	Xenon lamp, $\lambda \ge 420 \text{ nm}$	Reagent	0_0.0	2020)
3	g - C_3N_4	$0.05~\mathrm{g}$	Xenon lamp,	Indophenol	93.1	(E. Liu et al.,
			$\lambda > 420 \text{ nm}$ (14 Wm^2)	blue		2015)
4	$g-C_3N_4/Al_2O_3$	$0.1 \mathrm{~g}$	Two 13 W	Nessler	6.7	(Cui et al.,
			$\begin{array}{c} { m domestic} \\ { m energy-} \end{array}$	Reagent		2018)
			saving lamps			
5	$Bi_2O_2CO_3$ -g-	$0.1 \mathrm{\ g}$	300 W	Indophenol	250.6	(C. W. Wang,
	C_3N_4		Xenon lamp, $\lambda \ge 420 \text{ nm}$	blue		2017)
6	$\mathrm{Sb_2WO_6/g}$ -	$0.05~\mathrm{g}$	Xenon lamp	Ion chro-	63.0	(Cheng et al.,
	C_3N_4			matogra- phy		2021)
7	$Ag/g-C_3N_4$	$0.25~\mathrm{g}$	$300~\mathrm{W}$	Nessler	56.3	(Fu et al., 2019)
			Xenon lamp,	Reagent		
			$\lambda \geq 420 \text{ nm}$			
8	$g\text{-}C_3N_4/\mathrm{TiO}_2$	$0.2 \mathrm{~g}$	300 W	Ion chro-	78.6	(Nikokavoura
			Xenon lamp,	matogra-		and Trapalis,
			$\lambda \ge 420 \text{ nm}$	phy		2018)

Based on the data presented in Table 2, the photocatalytic performance of $Zr/g-C_3N_4$ (119.1 $\mu g L^{-1}h^{-1}g_cat^{-1}$) is notably lower than that of B-g-C₃N₄ (313.9 $\mu g L^{-1}h^{-1}g_cat^{-1}$) and Bi₂O₂CO₃/g-C₃N₄ (250.6 $\mu g L^{-1}h^{-1}g_cat^{-1}$) under similar operating conditions. Several factors may account for this difference. First, boron doping in g-C₃N₄ has been reported to introduce favorable mid-gap states, enhance electronic conductivity, and promote more efficient charge carrier separation, which facilitates higher photocatalytic activity for NO_x reduction (X. Li et al., 2020). In contrast, excessive Zr incorporation may lead to particle agglomeration or disruption of the g-C₃N₄ structure, reducing the number of accessible active sites and potentially creating recombination centers that hinder charge transfer (Zhao et al., 2021). Moreover, the heterojunction formed between g-C₃N₄ and

 ${\rm Bi_2O_2CO_3}$ in sample No.5 likely promotes more efficient interfacial charge separation and visible-light absorption due to the complementary band alignment (C. W. Wang, 2017), which may not be as effective in the ${\rm Zr/g\text{-}C_3N_4}$ system. These results reveal that Zr can enhance the performance of ${\rm g\text{-}C_3N_4}$ compared to pristine ${\rm g\text{-}C_3N_4}$, its effect is less pronounced than that of B or ${\rm Bi_2O_2CO_3}$ when incorporated with ${\rm g\text{-}C_3N_4}$ under comparable photocatalytic conditions.

4. Conclusion

In this study, a zirconium-incorporated graphitic carbon nitride ($\rm Zr/g-C_3N_4$) photocatalyst was successfully synthesized via pyrolysis and evaluated for its efficiency in NO_x reduction to ammonia. The photocatalyst was thoroughly characterized using X-ray diffraction (XRD), UV-Vis DRS, scanning electron microscopy (SEM)-EDX, and BET analysis, which confirmed structural modifications, enhanced light absorption, and improved surface properties due to Zr doping. Photocatalytic activity tests demonstrated that the $1\%\rm Zr/g-C_3N_4$ -400 catalyst achieved the highest ammonia yield of 119.1 $\mu\rm g/Lhg$, significantly outperforming undoped g-C₃N₄. The results revealed that moderate Zr doping improved charge separation and reduced electron-hole recombination, leading to enhanced photocatalytic performance. However, excessive calcination temperatures led to structural degradation and reduced ammonia production. These findings underscore the importance of optimizing dopant concentration and synthesis conditions to achieve superior photocatalytic efficiency. This study confirms that $\rm Zr/g-C_3N_4$ is a promising photocatalyst for sustainable NO_x-to-ammonia conversion, offering a potential pathway for environmental remediation and renewable energy applications.

Acknowledgements

This research was funded by ITB research grant under PPMI 2024 Program (Grant No. 1K/IT1.C07/SK-KP/2024). The authors also acknowledge the support from the Design Method and Process Control Laboratory, Department of Chemical Engineering, Institut Teknologi Bandung. The authors express their gratitude for the support from Nanoscience and Nanotechnology Research Centre (PPNN) ITB.

Conflict of Interest

The authors declare no conflicts of interest

References

- Astuti, Y., Amri, D., Widodo, D. S., Widiyandari, H., Balgis, R., & Ogi, T. (2020). Effect of fuels on the physicochemical properties and photocatalytic activity of bismuth oxide, synthesized using solution combustion method. *International Journal of Technology*, 11(1), 26–36. https://doi.org/10.14716/ijtech.v11i1.3342
- Cheng, L., Zhang, H., Li, X., Fan, J., & Xiang, Q. (2021). Carbon–graphitic carbon nitride hybrids for heterogeneous photocatalysis. *Small*, 17, 2005231. https://doi.org/10.1002/smll.202005231
- Cui, X., Tang, C., & Zhang, Q. (2018). A review of electrocatalytic reduction of dinitrogen to ammonia under ambient conditions. *Advanced Energy Materials*, 8, 1800369. https://doi.org/https://doi.org/10.1002/aenm.201800369
- Fidan, T., Torabfam, M., Saleem, Q., Wang, C., Kurt, H., Yüce, M., Tang, J., & Bayazit, M. K. (2021). Functionalized graphitic carbon nitrides for environmental and sens-

- ing applications. Advanced Energy and Sustainability Research, 2(1), 2000273. https://doi.org/10.1002/aesr.202000073
- Fu, J., Xu, Q., Low, J., Jiang, C., & Yu, J. (2019). Ultrathin 2d/2d wo3/g- $C_3N_4step-schemeH_2-production photocatalyst. Applied Catalysis B: Environmental, 243, 556–565. https://doi.org/10.1016/j.apcatb.2018.11.011$
- Gu, Z., Zhang, B., Asakura, Y., Tsukuda, S., Kato, H., Kakihana, M., & Yin, S. (2020). Alkali-assisted hydrothermal preparation of g- C_3N_4 /rgo nanocomposites with highly enhanced photocatalytic NO_x removal activity. Applied Surface Science, 521, 146213. https://doi.org/10.1016/j.apsusc.2020.146213
- Henderson-Sellers, A. (2013). *The climate modelling primer* (4th). Wiley Blackwell. https://www.wiley.com/en-us/The+Climate+Modelling+Primer%2C+4th+Edition-p-9781119943372
- Intergovernmental Panel on Climate Change. (2007). Climate change 2007: The physical science basis. contribution of working group i to the fourth assessment report of the intergovernmental panel on climate change (S. Solomon, D. Qin, M. Manning, Z. Chen, M. Marquis, K. B. Averyt, M. Tignor, & H. L. Miller, Eds.). Cambridge University Press. https://www.ipcc.ch/report/ar4/wg1/
- Khan, M. M., Ansari, S. A., Pradhan, D., & Ansari, M. O. (2015). Photocatalytic application of TiO_2 for the removal of pollutants from water. Arabian Journal of Chemistry, 8(5), 749–765. https://doi.org/10.1016/j.arabjc.2014.02.003
- Khanal, V., Balayeva, N., Günnemann, C., Mamiyev, Z., Dillert, R., Bahnemann, D. W., & Subramanian, V. R. (2021). Photocatalytic NO_x removal using tantalum oxide nanoparticles: A benign pathway. Applied Catalysis B: Environmental, 291, 119974. https://doi.org/10.1016/j.apcatb.2021.119974
- Kusdianto, K., Widiyastuti, W., Shimada, M., Nurtono, T., Machmudah, S., & Winardi, S. (2019). Photocatalytic activity of ZnO–Ag nanocomposites prepared by a one-step process using flame pyrolysis. *International Journal of Technology*, 10(3), 571–581. https://doi.org/10.14716/ijtech.v10i3.2902
- Li, G., Guo, J., Hu, Y., Wang, Y., Wang, J., Zhang, S., & Zhong, Q. (2021). Facile synthesis of the z-scheme graphite-like carbon nitride/silver/silver phosphate nanocomposite for photocatalytic oxidative removal of nitric oxides under visible light. *Journal of Colloid and Interface Science*, 588, 110–121. https://doi.org/10.1016/j.jcis.2020. 12.063
- Li, H., Zhao, Y., Tang, Q., & Wu, X. (2023). Thermal stability and photocatalytic degradation activity of $g C_3N_4$ under various calcination temperatures. *Applied Catalysis B: Environmental*, 326, 122385. https://doi.org/10.1016/j.apcatb.2023.122385
- Li, X., Chen, G., Yang, L., Jin, Z., & Wang, X. (2020). Photocatalytic NO removal over $g C_3N_4$ -based materials: Recent advances and future perspective. Chemical Engineering Journal, 382, 122842. https://doi.org/10.1016/j.cej.2019.122842
- Liu, E., Qi, L., Bian, J., Chen, Y., Hu, X., Fan, J., Liu, H., Zhu, C., & Wang, Q. (2015). A facile strategy to fabricate plasmonic Cu-modified TiO₂nano flowerfilmsforphotocatalytic reduction of CO2 tomethanol. Materials Research Bulletin, 68, 203–209. https://doi.org/10.1016/j.materresbull.2015.03.064
- Liu, Z., Wang, C., Zhu, Z., Lou, Q., Shen, C.-L., Chen, Y., Sun, J., Ye, Y., Zhang, J., Dong, L., & Shan, C.-X. (2021). Wafer-scale growth of two-dimensional graphitic carbon nitride films. *Matter*, 4, 162–168. https://doi.org/10.1016/j.matt.2021.02.014
- Mariyappillai, V., Shiyamala, C., Abisheik, T., Tiffany, M., Pandiyan, V., Senthilraja, A., Afzal, M., Barmavatu, P., Shanmugaraj, K., & Balu, K. (2025). Zr-modified ZnO nanoparticles: Optimized photocatalytic degradation and antibacterial efficiency

- for pollution control. Ceramics International, 51(17), 23003–23020. https://doi.org/https://doi.org/10.1016/j.ceramint.2025.02.402
- Mou, H., Yu, L., Zhang, H., Wu, Y., Wang, J., Yang, Y., Liu, X., & Wu, Z. (2019). Fabricating amorphous g-C3N4/ZrO2 photocatalysts by one-step pyrolysis for solar-driven ambient ammonia synthesis. *ACS Applied Materials & Interfaces*, 11 (47), 44360–44365. https://doi.org/10.1021/acsami.9b16786
- Muktaridha, O., Adlim, M., Suhendrayatna, S., Ismail, I., & Abu Bakar, N. H. H. (2021). Photocatalytic degradation of skim-latex-vapor odor using iron-doped zinc oxide. *International Journal of Technology*, 12(4), 739–748. https://doi.org/10.14716/ijtech.v12i4.4227
- Mutiara, S., Saputera, W. H., Devianto, H., & Sasongko, D. (2023). Recent advances on the utilization of TiO₂-based catalysts in the photocatalytic reduction of co to methane. *ChemistrySelect*, 10(20), e202302536. https://doi.org/10.1002/slct. 202302536
- Mutiara, S., Saputera, W. H., Utomo, W. P., Chung, H. Y., Abdi, F. F., Devianto, H., & Sasongko, D. (2024). Harnessing light and co with copper–nickel on TiO₂ photocatalysts for methanol production. *ChemCatChem*, 16(19), e202400583. https://doi.org/10.1002/cctc.202400583
- Nikokavoura, A., & Trapalis, C. (2018). Graphene and g-C3N4-based photocatalysts for NOx removal: A review. *Applied Surface Science*, 430, 18–52. https://doi.org/10.1016/j.apsusc.2017.08.192
- Nosaka, Y., & Nosaka, A. Y. (2017). Generation and detection of reactive oxygen species in photocatalysis. *Chemical Reviews*, 117(17), 11302–11336. https://doi.org/10.1021/acs.chemrev.7b00161
- Pahi, S., Barik, A., Sahoo, C., Rout, K., & Parida, K. (2021). Visible light active zrand n-doped TiO₂ coupled g-C₃N₄ heterojunction nanosheets as a photocatalyst for degradation. *Nanoscale Advances*, 3(22), 6468–6481. https://doi.org/10.1039/D1NA00517E
- Paul, D. R., Sharma, R., Nehra, S. P., & Sharma, A. (2019). Effect of calcination temperature, ph and catalyst loading on photodegradation efficiency of urea derived graphitic carbon nitride towards methylene blue dye solution. RSC Advances, 9(26), 15381–15389. https://doi.org/10.1039/C9RA02201E
- Qu, A., Xu, X., Xie, H., Zhang, Y., Li, Y., & Wang, J. (2016). Effects of calcining temperature on photocatalysis of g-C₃N₄/TiO₂ composites for hydrogen evolution from water. *Materials Research Bulletin*, 80, 167–176. https://doi.org/10.1016/j.materresbull.2016.03.043
- Rahma, F. N., & Hidayat, A. (2023). Biodiesel production from free fatty acid using zro2/bagasse fly ash catalyst. *International Journal of Technology*, 14(1), 206–218. https://doi.org/10.14716/ijtech.v14i1.4873
- Saputera, W. H., Yuniar, G., & Sasongko, D. (2024). Light-driven methane conversion: Unveiling methanol using a $TiO_2/tiof2$ photocatalyst. RSC Advances, 14, 8740–8751. https://doi.org/10.1039/d4ra00353e
- Sun, R., Peng, X., Yu, D., & Chen, Y. (2023). Band structure tuning of zr/C₃N₄ photocatalysts via thermal processing for enhanced visible-light activity. *Journal of Materials Chemistry A*, 11(12), 5802–5811. https://doi.org/10.1039/D3TA00652K
- Wahyudi, F., Saputera, W. H., Sasongko, D., & Devianto, H. (2023). Recent advances in the development of photocatalytic technology for nitrate reduction to ammonia. Case Studies in Chemical and Environmental Engineering, 8, 100478. https://doi.org/10.1016/j.cscee.2023.100478

- Wang, C. W. (2017). Recent advances of graphitic carbon nitride-based structures and applications in catalyst, sensing, imaging, and leds. *Nano-Micro Letters*, 8, 21–22. https://doi.org/10.1007/s40820-017-0148-2
- Wang, Y., Liu, Z., Chen, W., & Feng, H. (2023). Effect of zro particle sintering on the photocatalytic no reduction efficiency of zr/g-C₃N₄ composites. *Journal of Environmental Chemical Engineering*, 11(2), 109833. https://doi.org/10.1016/j.jece. 2023.109833
- Whulanza, Y., Kusrini, E., Hermansyah, H., Sudibandriyo, M., Sahlan, M., & Kartohardjono, S. (2024). Catalyzing clean energy: The role of hydrogen and ammonia technology processes. *International Journal of Technology*, 15(4), 803–811. https://doi.org/10.14716/ijtech.v15i4.7171
- Yang, H., Zhang, W., Chen, Y., & Sun, C. (2019). Modified langmuir-hinshelwood model for no photocatalytic degradation on semiconductors: A review. *Environmental Science: Nano*, 6(7), 2021–2035. https://doi.org/10.1039/C9EN00330J
- Yang, M., & Xu, Y.-J. (2014). Visible-light-driven photocatalysis on graphene-based materials. *Journal of Materials Chemistry A*, 2(29), 10733–10753. https://doi.org/10.1039/C4TA00957A
- Yi, J., El-Alami, W., Song, Y., Li, H., Ajayan, P. M., & Xu, H. (2019). Emerging surface strategies on graphitic carbon nitride for solar-driven water splitting. *Chemical Engineering Journal*, 382, 122812. https://doi.org/10.1016/j.cej.2019.122812
- Yu, M., Chang, S., Ma, L., Wu, X., Yan, J., Ding, Y., Zhang, X., Carabineiro, S., & Lv, K. (2025). Remarkable improvement in photocatalytic activity of g-C3N4 for NO oxidation through surface hydroxylation. Separation and Purification Technology, 354(1), 128695. https://doi.org/https://doi.org/10.1016/j.seppur.2024.128695
- Yu, Q., & Brouwers, H. J. H. (2009). Indoor air purification using heterogeneous photocatalytic oxidation. part i: Experimental study. *Applied Catalysis B: Environmental*, 92, 454–461. https://doi.org/10.1016/j.apcatb.2009.09.004
- Zhang, J., Zhu, Z., Tang, Y., & Leung, D. Y. C. (2014). Photocatalytic degradation of $NO_x usingg C_3N_4$: Effects of morphology and reaction mechanism. *Applied Catalysis B: Environmental*, 160–161, 408–415. https://doi.org/10.1016/j.apcatb. 2014.05.010
- Zhang, L., Jin, Z., Huang, S., Zhang, Y., Zhang, M., Zeng, Y.-J., & Ruan, S. (2019). Ce-doped graphitic carbon nitride derived from metal-organic frameworks as a visible light-responsive photocatalyst for H_2 production. Nanomaterials, 9(11), 1539. https://doi.org/10.3390/nano9111539
- Zhang, X., Kong, R. M., Du, H., Xia, L., & Qu, F. (2018). Highly efficient electrochemical ammonia synthesis via nitrogen reduction reactions on a vn nanowire array under ambient conditions. *Journal of Chemical*, 54, 5323–5325. https://doi.org/10.1039/C8CC00459E
- Zhanyong, Y., Jin, M., Wang, X., Zhi, R., Yang, J., Hao, H., Zhang, S., Zhou, E., & Yin, S. (2023). Recent advances in g-C₃N₄-based photocatalysts for NO_x removal. Catalysts, 13(1), 132–192. https://doi.org/10.3390/catal13010192
- Zhao, Y., Wang, Y., & Chen, F. (2021). Toward sustainable nitrogen cycle: Recovery of ammonia from NO_x via photocatalysis. Chemical Engineering Journal, 420, 127655. https://doi.org/10.1016/j.cej.2020.127655
- Zhou, M., Ou, H., Li, S., Qin, X., Fang, Y., Lee, S., Wang, X., & Ho, W. (2021). Photocatalytic air purification using functional polymeric carbon nitrides. *Journal of Science*, 8, 210–237. https://doi.org/10.1002/advs.202102376